

I2I-Mamba: Multi-modal medical image synthesis via selective state space modeling

Omer F. Atli^{a,b,e}, Bilal Kabas^{a,b}, Fuat Arslan^{a,b}, Arda C. Demirtas^{a,b}, Mahmut Yurt^c, Onat Dalmaz^c, Tolga Çukur^{a,b,d,*}

^aDepartment of Electrical and Electronics Engineering, Bilkent University, Ankara 06800, Turkey

^bNational Magnetic Resonance Research Center (UMRAM), Bilkent University, Ankara 06800, Turkey

^cDepartment of Electrical Engineering, Stanford University, CA 94305, United States

^dDepartment of Neuroscience, Bilkent University, Ankara 06800, Turkey

^eTürk Telekom R&D Department, Ankara, Türkiye

ARTICLE INFO

Keywords: medical image synthesis, modality, imputation, state space, Mamba

ABSTRACT

Multi-modal medical image synthesis involves nonlinear transformation of tissue signals between source and target modalities, where tissues exhibit contextual interactions across diverse spatial distances. As such, the utility of a network architecture in synthesis depends on its ability to express these contextual features. Convolutional neural networks (CNNs) offer high local precision at the expense of poor sensitivity to long-range context. While transformers promise to alleviate this issue, they suffer from an unfavorable trade-off between sensitivity to long- versus short-range context due to the intrinsic complexity of attention filters. To effectively capture contextual features while avoiding the complexity-driven trade-offs, here we introduce a novel multi-modal synthesis method, I2I-Mamba, based on the state space modeling (SSM) framework. Focusing on semantic representations across a hybrid residual architecture, I2I-Mamba leverages novel dual-domain Mamba (ddMamba) blocks for complementary contextual modeling in image and Fourier domains, while maintaining spatial precision with convolutional layers. Diverting from conventional raster-scan trajectories, ddMamba leverages novel SSM operators based on a spiral-scan trajectory to learn context with enhanced radial coverage and angular isotropy, and a channel-mixing layer to aggregate context across the channel dimension. Comprehensive demonstrations on multi-contrast MRI and MRI-CT protocols indicate that I2I-Mamba offers superior performance against state-of-the-art CNNs, transformers and SSMs.

1. Introduction

Multi-modal medical images with distinct tissue contrasts provide complementary information about underlying anatomy, boosting performance and reliability in downstream analyses (Pichler et al., 2008). Multi-modal imaging is viable using different sequences on the same scanner or on entirely different scanners, albeit costs of running prolonged exams yield incomplete protocols under many clinical scenarios (Thukral, 2015). As a remedy, target-modality images missing from a protocol can be synthesized based on the subset of source-modality images available (Iglesias et al., 2013; Huo et al., 2018). Key clinical applications of image synthesis include imputing target modalities that offer high diagnostic redundancy but are omitted from imaging protocols to reduce scan time and improve efficiency; inferring invasive target modalities from non-invasive sources to avoid exposure to ionizing radiation or harmful contrast agents (Lee et al., 2019); and recovering missing modalities

to enhance protocol consistency across participants in retrospective imaging studies (Clark et al., 2019). Yet, such synthesis tasks involve a challenging nonlinear transformation of signal levels between source and target images depending on tissue characteristics (Lee et al., 2017). Although detailed tissue parameters that govern signal levels are generally difficult to infer from medical images, multi-modal synthesis can be guided via a rudimentary spatial prior on tissue composition that can be implicitly inferred from the signal distribution in source images (Huang et al., 2017). Note that both healthy and pathological tissues can exhibit broad spatial distribution in the form of contiguous or segregated clusters across an anatomy (Adam et al., 2014), introducing not only local signal correlations in compact neighborhoods but also non-local signal correlations over extended distances. Thus, successful solution of a multi-modal synthesis task inherently rests on the ability to capture these short- and long-range contextual features in medical images.

Deep learning has recently emerged as the mainstream framework for medical image synthesis given its prowess in nonlinear function approximation (Vemulapalli et al., 2015;

*Corresponding author: Tolga Çukur, cukur@ee.bilkent.edu.tr

Wu et al., 2016; Alexander et al., 2014; Huynh et al., 2016). In learning-based synthesis, a neural network model attempts to map source onto target images through hierarchical nonlinear transformations on intermediate feature maps (Zhao et al., 2017; Chartsias et al., 2018). Naturally, the fidelity of this mapping depends on the model’s expressiveness for the diverse set of contextual features in medical images. Earlier studies have used CNN-based models with convolution operators for local filtering of feature maps (Bowles et al., 2016; Chartsias et al., 2018; Joyce et al., 2017; Yang et al., 2020; Wei et al., 2019). The popularity of CNNs has been fueled by linear model complexity with respect to image dimensionality, and high expressiveness for local context that can be critical in synthesis of detailed tissue structure (Beers et al., 2018; Dar et al., 2019; Yu et al., 2018, 2019; Nie et al., 2018; Armanious et al., 2019; Lee et al., 2019; Li et al., 2019; Zhou et al., 2020; Wang et al., 2020; Yurt et al., 2021). However, convolution operators have strictly localized spatial footprints, inducing poor sensitivity to long-range contextual features (Zhang et al., 2022; Korkmaz et al., 2023). In turn, CNNs can suffer from low synthesis accuracy near regions of heterogeneous tissue composition and uncommon pathology, where contextual relations often serve a key role in inferring the spatial distribution of tissue signals (Oktay et al., 2018; Lan et al., 2020).

Later studies have instead adopted transformer-based models based on self-attention operators that are capable of non-local filtering (Shin et al., 2020; Zhang et al., 2022; Dalmaz et al., 2022; Liu et al., 2023; Li et al., 2023). Tokenizing an input image as a sequence of patches, transformers compute attention weights to measure inter-patch similarity and non-locally filter the input sequence. While the diffuse spatial footprints of self-attention operators help increase sensitivity to long-range context, they induce quadratic model complexity with respect to sequence length (i.e., number of image patches), which can prohibit their use on small patches necessary to maintain high spatial precision, and compromise their learning efficiency on moderate-size datasets typically available in medical imaging (Liu et al., 2023; Li et al., 2023). Common strategies to facilitate use of transformers in imaging tasks include efficient attention operators that compress contextual representations at the expense of limiting contextual sensitivity (Zhang et al., 2022; Bedel et al., 2023), and tokenization via large patches (e.g., a 16×16 image patch taken as a single token) that compromises spatial precision (Dalmaz et al., 2022; Liu et al., 2023). As such, transformer-based methods typically face an undesirable trade-off between contextual sensitivity and spatial precision. An emerging alternative to efficiently capture contextual representations is state-space models (SSM) (Zhu et al., 2024; Liu et al., 2025). SSMs cast image pixels onto an input sequence via raster-scan trajectories in rectilinear orientations, and efficiently model this sequence via state-space operators that offer a refined trade-off between long- and short-range contextual sensitivity. Recent reports have already adopted selective SSMs (Mamba) for several unimodal analysis and reconstruction tasks in medical imaging (Ma et al., 2024; Huang et al., 2025; Korkmaz and Patel, 2025).

Given their success in other imaging tasks, SSMs hold signif-

icant promise for multi-modal medical image synthesis. However, several limitations hinder the effectiveness of existing SSMs in missing modality imputation. *Traditional SSMs perform recurrent sequence modeling directly in the image domain* to aggregate contextual information, which often leads to an inevitable trade-off between capturing short- and long-range dependencies—*global context is attenuated* due to the difficulty of modeling interactions between distant sequence elements (Ma et al., 2024). Moreover, multi-modal images of the same anatomy typically exhibit *signal correlations that vary with spatial frequency*: high-frequency edge structures are typically well-aligned across modalities, while low-frequency contrast information tends to be more modality-specific (Bilgic et al., 2011). Conventional image-domain SSMs can *struggle to model this frequency-dependent behavior* effectively, limiting their ability to capture cross-modal interactions. Finally, SSMs typically impose a *rectilinear raster-scan trajectory* (e.g., *sweep, zig-zag*) to sequentialize images, resulting in anisotropic receptive fields and *reduced sensitivity to contextual interactions along non-axial directions* (Korkmaz and Patel, 2025). Note that diagnostically relevant structures such as vasculature, cortical folds, and tumor lesions often follow oblique orientations that are poorly captured by rectilinear scans. These limitations collectively constrain the potential of SSMs in medical image synthesis tasks.

In this study, we present I2I-Mamba, a novel learning-based model for multi-modal medical image synthesis, designed to achieve high contextual sensitivity and spatial precision while addressing key limitations of existing SSM approaches (see Atli et al. (2024) for a preliminary version). The I2I-Mamba architecture incorporates dual-domain Mamba (ddMamba) blocks, residually fused with CNN blocks across a bottleneck that preserves high-resolution semantic representations (Fig. 1). To overcome the limitations of conventional image-domain SSMs in capturing global context and frequency-dependent interactions, ddMamba blocks feature independent SSM branches operating in both the image and Fourier domains. This dual-domain design enables the state-space operators to leverage both spatial and spectral contextual cues. To mitigate the anisotropic spatial footprint introduced by traditional raster-scan trajectories, ddMamba blocks adopt a novel spiral scan trajectory, enhancing both radial coverage and angular isotropy in receptive fields (Fig. 2). Additionally, ddMamba blocks incorporate channel-mixing layers to enable context aggregation not only across spatial dimensions but also across channel dimensions of the feature maps. This architectural design allows I2I-Mamba to more comprehensively model rich cross-modal contextual interactions in medical images. We demonstrate the effectiveness of I2I-Mamba through extensive experiments on missing modality imputation in multi-contrast MRI and MRI-to-CT translation tasks. Our results show that I2I-Mamba consistently outperforms state-of-the-art CNN, transformer, and SSM-based models. The code is publicly available at: <https://github.com/icon-lab/I2I-Mamba>.

Contributions

- We develop, to our knowledge, the first application of

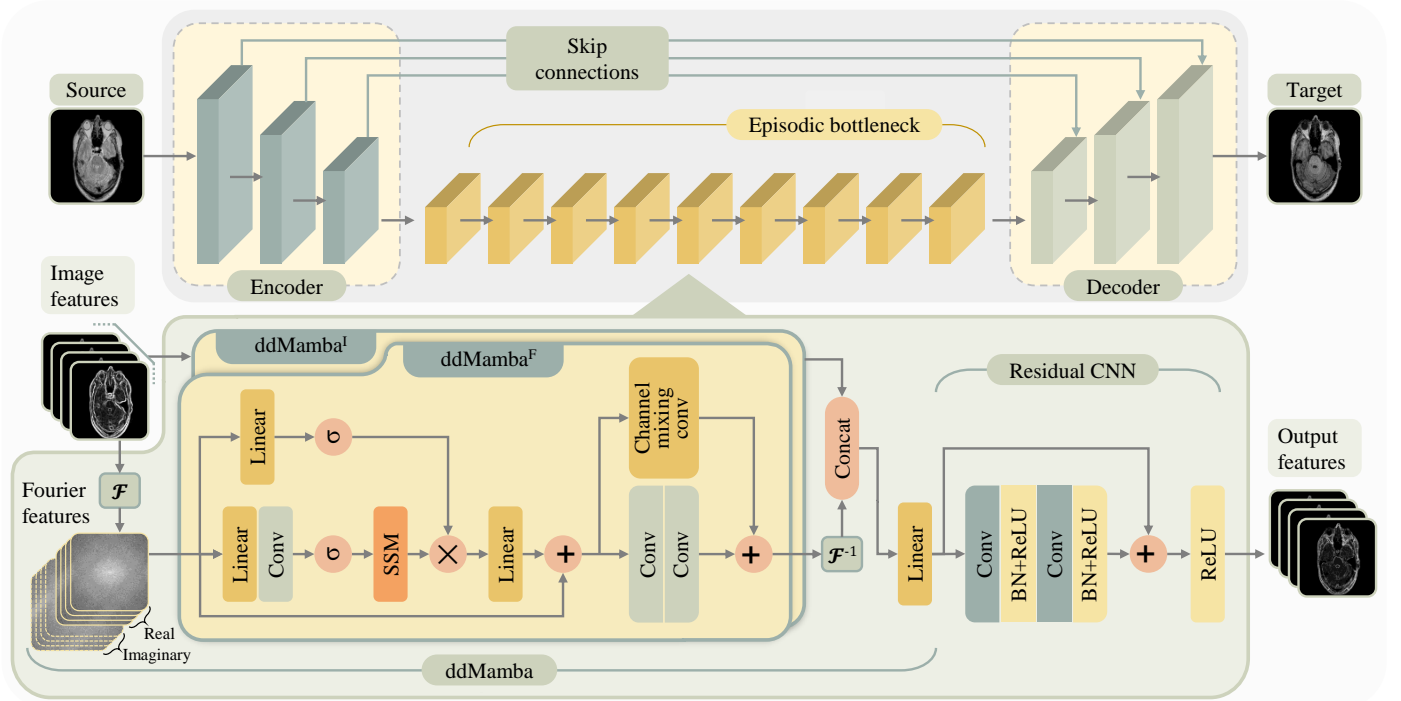


Fig. 1: Network architecture for I2I-Mamba. The proposed model comprises encoder, bottleneck, and decoder modules to synthesize target from source images. The encoder extracts high-level semantic representations of the source image via convolutional layers. The bottleneck extracts task-relevant contextual information across spatial, frequency and channel dimensions with the aid of dual-domain Mamba (ddMamba) blocks (ddMamba^I: image domain, ddMamba^F: Fourier domain) comprising channel-mixing layers, and maintains high spatial precision with the aid of residual CNN blocks. The decoder back-projects the contextualized representations onto the target image via convolutional layers.

SSMs for translating between multi-modal data to synthesize medical images from missing modalities.

- We propose a novel SSM model that operates on image and Fourier representations to enhance medical image synthesis by capturing complementary spatial and spectral features.
- We design a novel ddMamba block that modulates SSM outputs with channel-mixing layers, enabling the model to jointly learn contextual dependencies across spatial-spectral and channel dimensions.
- We introduce a spiral-scan trajectory for image- and Fourier-domain SSM layers that enhanced radial coverage and angular isotropy in receptive fields, improving the modeling of contextual interactions.

2. Related Work

2.1. Learning-based medical image synthesis

Learning-based image synthesis methods rely on the choice of model architecture to infer mappings across modalities. CNNs have been a mainstream architecture, using convolution operators to extract local image context. However, they struggle to generalize to atypical anatomy and model long-range dependencies (Oktay et al., 2018). Attention mechanisms have been considered in CNN backbones to emphasize semantically relevant regions during synthesis (Lan et al., 2020; Zhao et al.,

2020; Yuan et al., 2020; Arslan et al., 2024). Yet, because these mechanisms multiplicatively gate features derived via convolution operators, they provide only a modest change in sensitivity to global context (Dalmaz et al., 2022).

Transformers have been increasingly adopted to explicitly model long-range interactions between spatially distant regions (Zhang et al., 2022). While powerful, pure transformer-based models incur high computational costs, which has led to the development of efficient variants using approximations such as windowed or low-rank attention (Zhang et al., 2022; Bedel et al., 2023). These approximations, however, limit the model’s ability to capture the full-scope of contextual interactions (Zhang et al., 2022). Alternatively, hybrid CNN-transformer architectures apply transformer modules only in low-resolution stages to reduce computation (Chen et al., 2024; Dalmaz et al., 2022), compromising local precision. Consequently, transformer-based methods often trade off local precision for broader context due to the inherent limitations of attention mechanisms.

2.2. SSM models in medical imaging

SSMs have recently emerged as promising alternatives for achieving a refined balance between short- and long-range sensitivity, without incurring high model complexity. In medical imaging, SSM models have recently been proposed for unimodal tasks such as segmentation (Ma et al., 2024), reconstruction from undersampled measurements (Huang et al., 2025; Korkmaz and Patel, 2025), and unconditional generation (Ju and Zhou, 2024). However, these studies have not addressed the

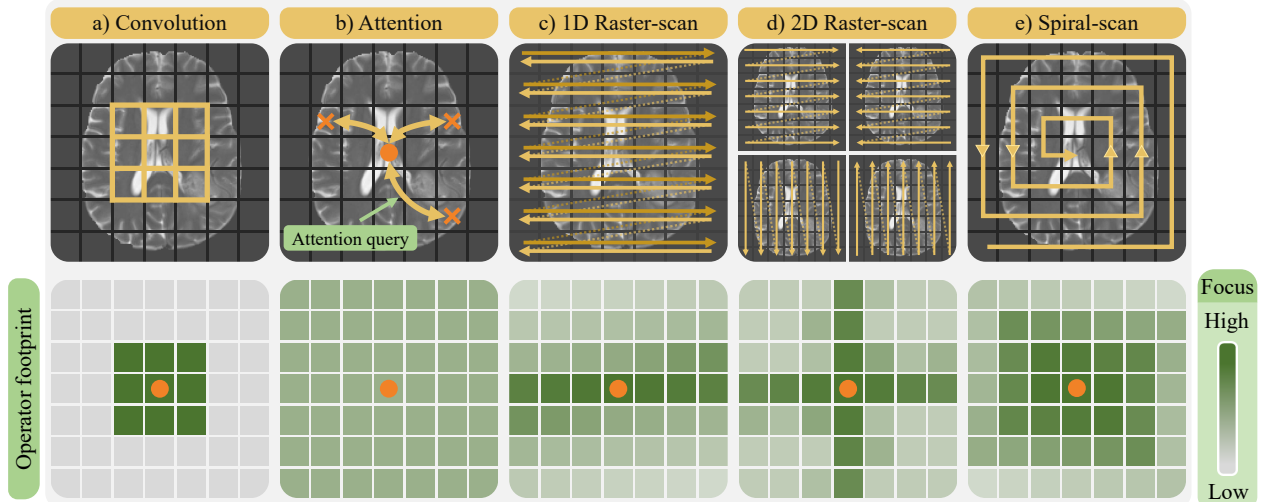


Fig. 2: Footprints illustrating the spatial distribution of focus that each learning operator deploys (see colorbar), while seeking contextual interactions of a central pixel (orange dots). **(a)** Convolution operators in CNNs have localized footprints with heavy focus over a restricted neighborhood, compromising sensitivity to long-range contextual interactions. **(b)** Attention operators in transformers have non-local footprints that diffusely distribute focus over the image, compromising local precision. **(c), (d)** Conventional state-space operators in SSMs are based on multiple raster-scan trajectories with anisotropic footprints biased towards rectangular image axes, limiting sensitivity to interactions in non-axial orientations. **(e)** I2I-Mamba’s state-space operator leverages a novel spiral-scan trajectory that attains a near-isotropic footprint with more uniform focus across orientations, maintaining an improve balance between long- versus short-range contextual interactions.

distinct challenges posed by multi-modal synthesis. Here we introduce I2I-Mamba, the first SSM-based framework specifically designed for mapping between distinct imaging modalities to our knowledge—including both multi-contrast MRI and MRI-to-CT translation. Conventional UNet-style SSM architectures typically reduce spatial resolution to coarse feature maps (e.g., 16×16) (Liu et al., 2025), thereby limiting spatial precision in contextual modeling (Dar et al., 2019). Furthermore, conventional SSM models often operate solely in the image domain, making them less effective at capturing frequency-dependent patterns and long-range global structures. These models also use raster-scan trajectories to map images into 1D sequences, which introduces anisotropic biases in horizontal and vertical directions (Liu et al., 2025). I2I-Mamba departs from existing SSM architectures in imaging in several ways. First, it employs a deep latent bottleneck at higher resolution (64×64), preserving local spatial detail while enabling efficient contextualization. Second, it uses dual-domain SSM processing, jointly operating in both image and Fourier domains. This dual representation enables state-space operators to simultaneously learn spatially localized features and globally coherent spectral patterns, offering improved sensitivity to multi-scale and frequency-aware features. Third, we propose a spiral-scan trajectory for SSM tokenization, yielding near-isotropic receptive fields and mitigating directional bias in contextual modeling. These technical advances position I2I-Mamba as a performant solution for modality translation in medical imaging.

Following the release of our preprint (Atli et al., 2024), we became aware of an independent effort on multi-contrast MRI synthesis that applies conventional SSMs operating in image domain with raster-scan trajectories, in combination with transformers (Chen et al., 2025). Differently from Chen et al. (2025), we propose a hybrid SSM-CNN architecture that does not

contain any transformer modules, we introduce dual-domain SSM modules instead of conventional image-domain SSMs, we leverage spiral-scan tokenization instead of raster scans, and we devise I2I-Mamba for multi-model translation tasks beyond multi-contrast MRI. Despite differences in both architecture and scope of applications, this independent effort further underscores the relevance of SSMs for multi-modal synthesis.

2.3. Multi-domain processing in medical image synthesis

Multi-domain processing has remained relatively underexplored in medical image synthesis. Existing methods largely operate in the image domain, with limited attention to complementary transform-based representations. A recent study has investigated the multi-resolution nature of wavelets to capture hierarchical image features (Friedrich et al., 2025). However, the wavelet-domain method is based on a convolutional backbone, hence does not benefit from the contextual modeling capabilities of state-space operators in transform domains. To our knowledge, I2I-Mamba is the first to employ SSM in a dual-domain formulation, where image- and Fourier-domain representations are processed in parallel. This dual-domain design enables context fusion across spatial and spectral representations, offering a principled way to integrate localized and global structural contents.

3. Methods

3.1. I2I-Mamba

I2I-Mamba is a novel medical image synthesis model that combines the contextual sensitivity of SSMs with the local precision of CNNs for improved performance in multi-modal medical image synthesis. Details of the proposed architecture and learning procedures are described below.

3.1.1. Model Architecture

Given the prowess of adversarial methods in image synthesis (Dar et al., 2019), I2I-Mamba is devised as an adversarial model with generator/discriminator subnetworks. The generator comprises encoder, episodic bottleneck, and decoder modules to synthesize target-modality images from source-modality images (Fig. 1).

Encoder. Receiving as input available source-modality images, the encoder extracts high-level latent representations after concatenating input modalities into a tensor:

$$X = [x_1; x_2; \dots; x_I], \quad (1)$$

where $I \in \mathbb{Z}^+$ is the number of source modalities, $x_i \in \mathbb{R}^{H,W}$ is the source image for the i th modality, and $X \in \mathbb{R}^{H,W,I}$ is the input tensor (H, W : image height and width). The input tensor is projected through multiple CNN blocks to derive latent representations at relatively high spatial resolution:

$$f_1 = \text{CNN}(X), \quad (2)$$

where $f_1 \in \mathbb{R}^{H'=H/\alpha, W'=W/\alpha, C}$ (α : moderate downsampling rate, C : the number of feature channels).

Dual-domain Mamba bottleneck. Next, a deep bottleneck with J stages extracts task-relevant contextual representations. At each stage, *novel ddMamba blocks* are employed that contain SSM layers independently operating in image and Fourier domains to capture spatial and spectral context (Fig. 1), followed by channel-mixing layers to aggregate contextual interactions among the channel dimension. The contextualized feature maps from the ddMamba blocks are further processed via a residual CNN (rCNN) block to maintain high spatial precision. Receiving the feature map $f_j \in \mathbb{R}^{H',W',C}$, the j th bottleneck stage computes $f_{j+1} \in \mathbb{R}^{H',W',C}$ as:

$$f_{j+1} = \text{rCNN}(\text{ddMamba}(f_j)). \quad (3)$$

In each ddMamba block, a first branch ddMamba^I derives feature map $e_{cm}^I \in \mathbb{R}^{H',W',C}$ operating in the image domain:

$$e_{cm}^I = \text{ddMamba}^I(f_j). \quad (4)$$

A second branch ddMamba^F derives feature map $e_{cm}^F \in \mathbb{R}^{H',W',C}$ operating in the Fourier domain:

$$e_{cm}^F = \mathcal{F}^{-1}\{\text{ddMamba}^F(\mathcal{F}\{f_j\})\}, \quad (5)$$

where $\mathcal{F}, \mathcal{F}^{-1}$ denote forward and inverse Fourier transformation, respectively. In ddMamba^F , real and imaginary components of complex feature maps $\mathcal{F}\{f_j\}$ resulting from Fourier transformation are stored across the channel dimension. The contextualized feature maps are concatenated and two-fold compressed in the channel dimension via a linear projection:

$$\tilde{e}_{cm} = \text{Lin}([e_{cm}^I; e_{cm}^F]), \quad (6)$$

which is forwarded to the rCNN block (He et al., 2016).

Within ddMamba branches, a gating variable $g \in \mathbb{R}^{H',W',C'}$ ($C' = \beta C$ for ddMamba^I , $C' = 2\beta C$ for ddMamba^F) is first computed as:

$$g = \sigma(\text{Lin}_\beta(f_j)), \quad (7)$$

where σ is an activation function, Lin has expansion factor β . The input feature map f_j (or $\mathcal{F}(f_j)$) is then embedded via depth-wise convolution, and passed through an SSM layer:

$$e_j = \sigma(\text{DWConv}(\text{Lin}_\beta(f_j))), \quad (8)$$

$$M = \text{SSM}(e_j). \quad (9)$$

Spiral-scan SSM operators. In conventional SSM layers, the input feature map is expanded along spatial dimensions onto a 1D sequence via multiple raster-scan trajectories (e.g., based on rectilinear sweep or zig-zag patterns) (Liu et al., 2025). This causes state-space operators to have anisotropic footprints biased towards rectangular image axes, which can compromise learning of contextual features in remaining orientations (Fig. 2c-d). To alleviate orientation bias in state-space operators, here we propose a *novel spiral-scan trajectory* that maps $e_j \in \mathbb{R}^{H',W',C'}$ onto a sequence z_{in} as (Fig. 2e):

$$z_{in}[n, c] = e_j(h[n], w[n], c), \quad \text{such that:} \quad (10)$$

$$h[n] = (1 - \Gamma) \lfloor \frac{H' + 2}{2} \rfloor + \sum_{k=1}^{(H'W' - n + 1)} \Gamma \cos(\frac{\pi}{2} \lfloor \sqrt{4k - 7} \rfloor),$$

$$w[n] = (1 - \Gamma) \lfloor \frac{W' + 2}{2} \rfloor - \sum_{k=1}^{(H'W' - n + 1)} \Gamma \sin(\frac{\pi}{2} \lfloor \sqrt{4k - 7} \rfloor).$$

where $n \in \mathbb{Z}^{[1, H'W']}$ is the sequence index, $\Gamma = \text{sgn}(k-1)$ with sgn denoting signum function, $\lfloor \cdot \rfloor$ is the floor operation, and $(h \in \mathbb{Z}^{[1, H]}, w \in \mathbb{Z}^{[1, W]})$ denote the ordering of rectangular pixel coordinates.

The sequence is then processed via the discretized state-space operator separately across channels (Liu et al., 2025):

$$\ell[n, c] = \bar{\mathbf{A}}\ell[n-1, c] + \bar{\mathbf{B}}[n]z_{in}[n, c], \quad (11)$$

$$z_{out}[n, c] = \bar{\mathbf{C}}[n]\ell[n, c], \quad (12)$$

where ℓ is the hidden state, $\bar{\mathbf{A}} \in \mathbb{R}^{N,N}$ is a learnable and $\bar{\mathbf{B}}[n] \in \mathbb{R}^{N,1}$, $\bar{\mathbf{C}}[n] \in \mathbb{R}^{1,N}$ are learnable, input-dependent parameters, N is the state dimensionality. By inverting the coordinate mapping in Eq. 10, the output sequence z_{out} is remapped onto feature map $M \in \mathbb{R}^{H',W',C'}$. After gating M via a Hadamard product, it is linearly projected and residually combined with f_j :

$$e_{\text{SSM}} = f_j + \text{Lin}_{1/\beta}(g \odot M). \quad (13)$$

Note that $e_{\text{SSM}} \in \mathbb{R}^{H',W',C'}$ primarily captures spatial or spectral relationships in feature maps, while treating channels independently. Thus, we propose to include a channel-mixing layer in ddMamba blocks to aggregate context across channels:

$$e_{cm} = \text{cmConv}(e_{\text{SSM}}) + \text{Conv}(e_{\text{SSM}}), \quad (14)$$

where channel mixing is achieved via a 1×1 convolution operator (Tolstikhin et al., 2021). Next, $\tilde{e}_{cm} \in \mathbb{R}^{H',W',C}$ fused across the ddMamba branches is projected through an rCNN block to compute the output feature map f_{j+1} .

Decoder. The decoder receives contextualized feature maps f_j from the bottleneck and projects them onto synthetic target image $y \in \mathbb{R}^{H,W}$ via transposed convolution blocks:

$$y = \text{CNN}_{\text{transposed}}(f_j). \quad (15)$$

Table 1: Performance for multi-contrast MRI synthesis tasks in IXI. PSNR (dB) and SSIM are listed as mean±std across the test set. Boldface indicates the top-performing model for each task.

	T ₁ , T ₂ → PD		T ₁ , PD → T ₂		T ₂ , PD → T ₁		T ₂ → PD		PD → T ₂	
	PSNR	SSIM	PSNR	SSIM	PSNR	SSIM	PSNR	SSIM	PSNR	SSIM
I2I-Mamba	33.46	0.969	34.59	0.970	29.15	0.947	32.59	0.967	33.89	0.968
	±2.52	±0.011	±2.03	±0.011	±2.48	±0.027	±2.48	±0.012	±1.65	±0.011
pGAN	31.40	0.948	31.96	0.955	27.14	0.928	30.86	0.957	30.11	0.949
	±2.40	±0.013	±1.95	±0.015	±2.45	±0.031	±2.39	±0.015	±2.34	±0.019
medSynth	30.69	0.940	32.66	0.963	27.10	0.915	29.10	0.909	30.41	0.956
	±2.43	±0.019	±2.40	±0.017	±2.18	±0.037	±2.44	±0.013	±2.08	±0.016
WDM	32.50	0.966	33.30	0.964	28.01	0.934	31.27	0.960	32.34	0.961
	±2.48	±0.011	±1.75	±0.012	±2.48	±0.033	±2.48	±0.014	±1.55	±0.012
PTNet	30.33	0.935	32.62	0.954	27.73	0.931	29.75	0.932	32.46	0.956
	±2.59	±0.018	±2.09	±0.013	±2.79	±0.029	±2.66	±0.012	±2.19	±0.022
ResViT	32.98	0.968	33.47	0.964	28.45	0.936	32.08	0.952	32.84	0.964
	±2.35	±0.027	±2.54	±0.014	±1.46	±0.011	±2.49	±0.010	±1.56	±0.011
TransUNet	30.84	0.953	32.36	0.960	27.34	0.928	29.01	0.927	31.73	0.958
	±2.27	±0.031	±1.97	±0.015	±1.95	±0.033	±2.37	±0.019	±1.87	±0.015
Swin-UNet	31.37	0.966	31.35	0.958	26.11	0.933	29.32	0.941	30.87	0.960
	±2.63	±0.011	±4.25	±0.039	±3.28	±0.036	±4.07	±0.049	±3.89	±0.035
U-Mamba	31.96	0.960	28.53	0.937	27.73	0.929	32.26	0.963	26.48	0.900
	±2.43	±0.012	±2.27	±0.030	±2.52	±0.040	±2.30	±0.014	±5.87	±0.098
Mamba-UNet	29.56	0.967	32.39	0.966	26.93	0.940	29.54	0.948	30.33	0.955
	±4.48	±0.016	±3.90	±0.035	±3.40	±0.037	±3.88	±0.046	±3.97	±0.035

3.1.2. Learning Procedures

I2I-Mamba is implemented as an adversarial model with a conditional patch-based discriminator D (Nie et al., 2018). D distinguishes between actual (y_{act}) and synthetic (y_{syn}) target images. A combined pixel-wise and adversarial objective is used to train the generator G (Dalmaz et al., 2022):

$$L_G = \lambda_{pix} \mathbb{E}[\|y_{syn} - y_{act}\|_1] - \lambda_{adv} \{\mathbb{E}[D(y_{act}|X)^2] + \mathbb{E}[(D(y_{syn}|X) - 1)^2]\}, \quad (16)$$

where \mathbb{E} denotes expectation, $y_{syn} = G(X)$, λ_{pix} and λ_{adv} are loss-term weightings. Meanwhile, an adversarial term is used to train the discriminator D (Nie et al., 2018):

$$L_D = \mathbb{E}[D(y_{act}|X)^2] + \mathbb{E}[(D(y_{syn}|X) - 1)^2]. \quad (17)$$

3.2. Datasets

Experiments were conducted on multi-contrast brain MRI datasets (IXI: <https://brain-development.org/ixi-dataset/>, BraTS (Baid et al., 2021)) and a multi-modal pelvic MRI-CT dataset (Nyholm et al., 2018).

IXI. T₁-, T₂-, PD-weighted MR images were analyzed with (7500, 3000, 5400) cross-sections reserved for (training, validation, test) sets, based on a subject-level split. Prior to modeling, T₂- and PD-weighted images were spatially registered onto T₁-weighted images in each subject via an affine transformation in FSL.

BraTS. T₁-, T₂-, FLAIR-weighted MR images from were analyzed with (7500, 3000, 7500) cross-sections reserved for (training, validation, test) sets, based on a subject-level split.

As publicly shared, this dataset provides images that are co-registered onto T₁-weighted MRI scans.

MRI-CT. T₁-, T₂-weighted MRI, and CT images from were analyzed with a (2430, 540, 1080) cross-section reserved for (training, validation, test) sets, based on a subject-level split. As publicly shared, this dataset provides multi-modal images that are co-registered onto T₂-weighted MRI scans.

3.3. Architectural Design

The encoder module in I2I-Mamba had 3 stages, each containing a CNN block with a convolutional layer, batch normalization, and ReLU activation. $H=256$, $W=256$, $\alpha=4$, $C=256$ were used. The bottleneck had 9 stages, each containing a residual CNN block with 2 cascades of a convolutional layer, batch normalization, and ReLU activation. Dual-domain ddMamba blocks were inserted in bottleneck stages $j=\{1,5,9\}$, and used $\beta=2$, $N=16$, and SiLU activations. Channel-mixing blocks used a parallel combination of a channel-mixing convolutional layer and 2 regular convolutional layers. The decoder module had 3 stages, each containing a CNN block with a convolutional layer, batch normalization, and ReLU activation, except for the final stage that used a Tanh activation. Long-range skip connections were employed between corresponding encoder-decoder stages to better preserve low-level spatial information.

3.4. Competing Methods

State-of-the-art baselines for medical image synthesis were considered including convolutional models (pGAN (Dar et al., 2019), medSynth (Nie et al., 2018), WDM (Friedrich et al., 2025)), transformer models (PTNet (Zhang et al., 2022)),

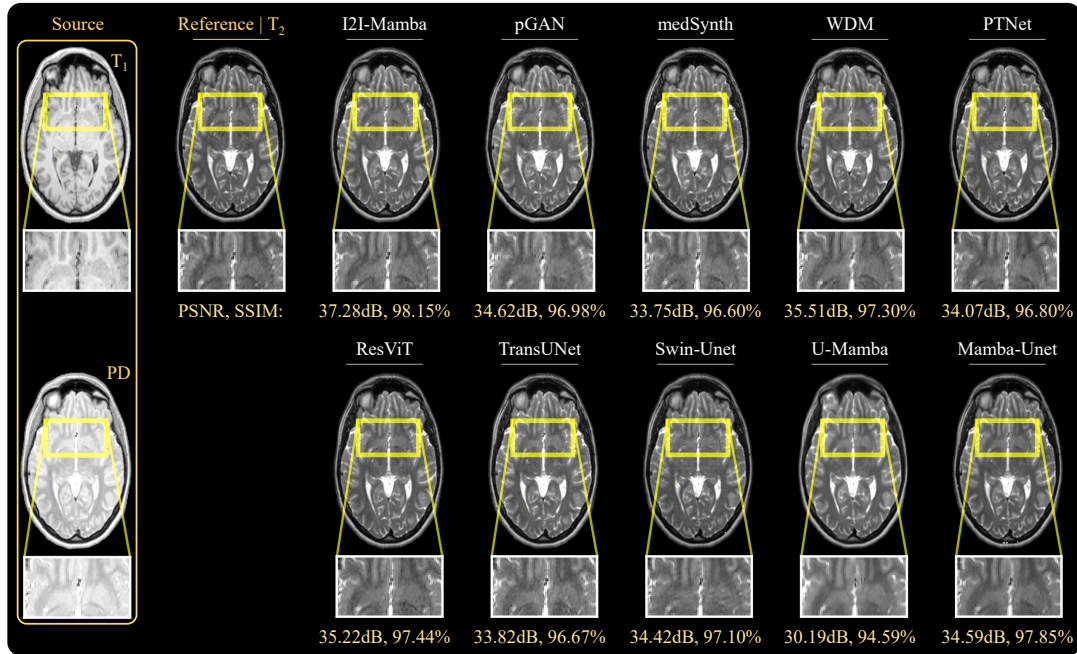


Fig. 3: Representative results for T₁, PD → T₂ in IXI. Synthetic target images from competing methods are displayed along with source images and reference target images. Zoom-in windows and error maps are also included to highlight differences among methods.

ResViT (Dalmaz et al., 2022), TransUNet (Chen et al., 2024), Swin-Unet (Cao et al., 2022), and recent SSM models introduced for medical image segmentation (U-Mamba (Ma et al., 2024), Mamba-Unet (Ma and Wang, 2024)). For fair comparison, all competing methods were implemented as adversarial models that processed individual cross-sections, and used a PatchGAN discriminator along with the losses in Eqs. 16-17.

3.5. Modeling Procedures

Modeling was performed using the PyTorch framework on an Nvidia RTX 4090 GPU. All models were trained from scratch via the Adam optimizer with parameters $\beta_1 = 0.5$, $\beta_2 = 0.999$. Model hyperparameters were selected via cross-validation. To avoid potential biases, a common set of hyperparameters observed to yield near-optimal validation performance across models was selected. Accordingly, 2×10^{-4} learning rate, 60 epochs, $\lambda_{adv} = 1$, $\lambda_{pix} = 100$ were prescribed. To evaluate performance, peak signal-to-noise ratio (PSNR) and structural similarity index (SSIM) metrics were measured between ground-truth and synthetic images. Significance of performance differences was assessed with non-parametric signed-rank tests ($p < 0.05$).

4. Results

4.1. Multi-Contrast MRI Synthesis

We first conducted experiments for target-modality imputation in multi-contrast MRI. I2I-Mamba was comparatively demonstrated against convolutional (pGAN, medSynth, WDM), transformer (PTNet, ResViT, TransUNet, Swin-Unet), and SSM (U-Mamba, Mamba-Unet) models. Table 1 lists performance metrics for synthesis tasks in IXI that comprises data

from healthy subjects. I2I-Mamba achieves the highest performance metrics consistently across tasks ($p < 0.05$). On average, I2I-Mamba offers performance improvements of 2.1dB PSNR, 1.7% SSIM over convolutional baselines including the wavelet-domain WDM method; 2.1dB PSNR, 1.5% SSIM over transformer baselines; and 3.2dB PSNR, 1.8% SSIM over SSM baselines. Meanwhile, Table 2 lists performance metrics for synthesis tasks in BraTS that comprises data from glioma subjects. I2I-Mamba again achieves the highest performance metrics in all tasks ($p < 0.05$), except for T₁, T₂ → FLAIR where medSynth yields similar SSIM and T₂, FLAIR → T₁ where TransUNet yields modestly higher SSIM. On average, I2I-Mamba offers performance improvements of 0.9dB PSNR, 1.0% SSIM over convolutional; 1.2dB PSNR, 1.7% SSIM over transformer; and 1.0dB PSNR, 1.6% SSIM over SSM baselines.

Synthetic target images from representative tasks are displayed in Fig. 3 for the IXI dataset, and in Fig. 4 for the BraTS dataset. Among competing methods, convolutional baselines suffer from residual noise (e.g., pGAN) or structural inaccuracies (e.g., medSynth, WDM); and transformer and SSM baselines suffer either from a degree of spatial blur and contrast loss (e.g., PTNet, U-Mamba, Mamba-UNet) or pixel intensity artifacts (ResViT, TransUNet, Swin-Unet) that lead to inaccuracies in depiction of detailed anatomical structures. Particularly evident in BraTS images containing pathology, baselines generally suffer from hallucinatory features manifesting as hypo-intense or hyper-intense signals deviating from ground truth. In comparison to baselines, I2I-Mamba synthesizes target images with more accurate depiction of detailed structure and contrast in tissues, along with lower artifacts.

Performance benefits of I2I-Mamba over SSM baselines can be attributed to the fundamental architectural differences between methods. Note that U-Mamba and Mamba-UNet fol-

Table 2: Performance for multi-contrast MRI synthesis tasks in BraTS.

	$T_1, T_2 \rightarrow \text{FLAIR}$		$T_1, \text{FLAIR} \rightarrow T_2$		$T_2, \text{FLAIR} \rightarrow T_1$		$T_2 \rightarrow \text{FLAIR}$		$\text{FLAIR} \rightarrow T_2$	
	PSNR	SSIM	PSNR	SSIM	PSNR	SSIM	PSNR	SSIM	PSNR	SSIM
I2I-Mamba	26.51 ± 2.37	0.911 ± 0.033	26.38 ± 2.18	0.913 ± 0.029	23.83 ± 3.79	0.904 ± 0.034	25.79 ± 2.44	0.903 ± 0.034	25.99 ± 2.13	0.908 ± 0.030
pGAN	25.50 ± 2.48	0.905 ± 0.031	25.47 ± 1.82	0.898 ± 0.029	23.01 ± 4.15	0.895 ± 0.036	24.52 ± 2.33	0.891 ± 0.033	25.11 ± 1.86	0.898 ± 0.030
medSynth	25.69 ± 2.25	0.911 ± 0.031	25.16 ± 1.79	0.894 ± 0.030	23.46 ± 3.17	0.902 ± 0.032	25.07 ± 2.26	0.889 ± 0.034	24.77 ± 1.70	0.890 ± 0.030
WDM	25.70 ± 2.36	0.901 ± 0.032	25.70 ± 1.85	0.903 ± 0.028	23.37 ± 3.53	0.900 ± 0.033	25.03 ± 2.40	0.893 ± 0.034	25.06 ± 1.92	0.896 ± 0.029
PTNet	25.03 ± 2.31	0.888 ± 0.038	24.52 ± 1.70	0.886 ± 0.032	20.94 ± 3.66	0.871 ± 0.044	24.45 ± 2.08	0.882 ± 0.037	23.89 ± 1.63	0.876 ± 0.033
ResViT	25.79 ± 2.16	0.900 ± 0.031	25.29 ± 1.74	0.904 ± 0.027	23.06 ± 3.48	0.899 ± 0.032	24.95 ± 2.11	0.883 ± 0.034	24.89 ± 1.72	0.888 ± 0.028
TransUNet	25.54 ± 2.24	0.899 ± 0.032	25.59 ± 1.86	0.909 ± 0.024	23.26 ± 3.52	0.907 ± 0.033	25.28 ± 2.26	0.896 ± 0.032	25.04 ± 1.84	0.899 ± 0.029
Swin-Unet	25.03 ± 2.14	0.887 ± 0.035	24.70 ± 1.90	0.886 ± 0.032	22.95 ± 3.31	0.887 ± 0.037	24.51 ± 2.54	0.879 ± 0.034	24.33 ± 1.74	0.881 ± 0.033
U-Mamba	25.37 ± 2.39	0.891 ± 0.037	25.58 ± 1.70	0.909 ± 0.026	23.36 ± 3.59	0.895 ± 0.035	24.86 ± 1.55	0.882 ± 0.022	25.03 ± 1.33	0.894 ± 0.024
Mamba-Unet	25.17 ± 1.93	0.892 ± 0.033	25.16 ± 1.83	0.893 ± 0.030	23.12 ± 2.28	0.889 ± 0.036	24.83 ± 2.10	0.883 ± 0.037	24.51 ± 1.93	0.889 ± 0.027

low a UNet-style architecture that substantially lowers spatial resolution of encoded feature maps, and they use conventional image-domain SSM operators based on raster-scan trajectories. In contrast, I2I-Mamba adopts a residual architecture where the bottleneck maintains relatively higher-resolution semantic representations, and it uses ddMamba blocks operating in image and Fourier domains, equipped with SSM operators based on spiral-scan trajectories. Our results indicate that these technical elements enable I2I-Mamba to sensitively capture of a comprehensive set of contextual features to synthesize high-quality target images in multi-contrast MRI protocols.

4.2. MRI-CT Synthesis

Next, we conducted experiments for target-modality imputation on the multi-modal MRI-CT dataset. Performance metrics for MRI \rightarrow CT synthesis tasks are listed in Table 3. Among competing methods, I2I-Mamba achieves the highest performance metrics consistently across tasks ($p < 0.05$). On average, I2I-Mamba attains improvements of 1.7dB PSNR, 2.0% SSIM over convolutional baselines; 1.8dB PSNR, 1.9% SSIM over transformer baselines; and 3.0dB PSNR, 2.8% SSIM over SSM baselines. Consistent with the findings in multi-contrast MRI synthesis, we observe that I2I-Mamba outperforms both the wavelet-domain convolutional baseline (WDM) and the SSM-based baselines (U-Mamba, Mamba-UNet), which rely on conventional image-domain SSM operators with raster-scan trajectories. These results collectively suggest that the dual-domain SSM operators in I2I-Mamba—operating jointly in the image and Fourier domains—enhance contextual sensitivity beyond what is achievable with wavelet-domain processing or standard image-domain SSMs. This elevated sensitivity to task-relevant

contextual features contributes to the improved reliability of I2I-Mamba in multi-modal medical image synthesis.

Representative synthetic images are displayed in Fig. 5. Among competing methods, convolutional baselines suffer from residual noise (e.g., pGAN, WDM) or structural degradations (e.g., medSynth). Meanwhile, transformer and SSM baselines suffers from spatial smoothing (e.g., ResViT, TransUNet, Swin-Unet, U-Mamba), hypo- or hyper-intense contrast compared to ground truth in regions near bone tissue (e.g., PTNet, U-Mamba), or dark-pixel artifacts (e.g., Swin-Unet, Mamba-Unet). In comparison, I2I-Mamba synthesizes target images with lower artifacts and more accurate delineation of tissue structure and contrast, particularly across diagnostically relevant bone regions. Taken together, these results indicate that I2I-Mamba maintains higher sensitivity to contextual features in multi-modal medical images than baselines, thereby increasing fidelity in imputation of missing modalities.

4.3. Computational Complexity

Inference times and memory load per cross-section for all competing methods are summarized in Table 4 along with model parameter counts. As expected, transformer-based models exhibit substantial computational overhead, reflected in longer inference times, higher memory usage, and increased parameter counts. This trend holds for both hybrid CNN-transformer architectures (e.g., ResViT, TransUNet) and more efficient transformer variants employing approximate attention mechanisms (e.g., PTNet, Swin-Unet). In contrast, convolutional baselines offer high computational efficiency, with pure image-domain architectures (e.g., pGAN, medSynth) demonstrating the lowest inference times and memory demands. SSM-based methods, including I2I-Mamba, exhibit notably

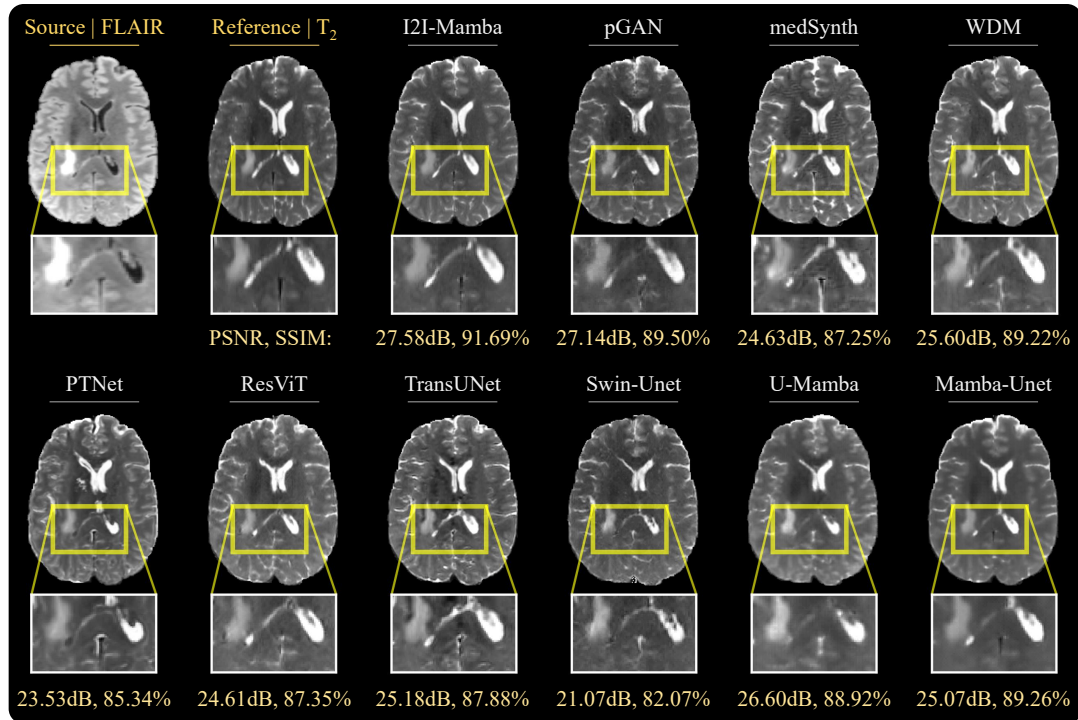


Fig. 4: Representative results for FLAIR \rightarrow T₂ in BraTS. Synthetic target images from competing methods are displayed along with source images and reference target images. Zoom-in windows and error maps are also included to highlight differences among methods.

Table 3: Performance for the T₂-MRI \rightarrow CT and T₁-MRI \rightarrow CT synthesis tasks in the MRI-CT dataset.

		I2I-Mamba	pGAN	medSynth	WDM	PTNet	ResViT	TransUNet	Swin-Unet	U-Mamba	Mamba-Unet
T ₂ \rightarrow CT	PSNR	28.47	24.64	26.87	26.83	27.35	27.87	28.06	24.14	26.32	24.66
		± 2.15	± 1.59	± 1.79	± 1.80	± 2.23	± 2.06	± 2.20	± 1.87	± 1.77	± 2.69
	SSIM	0.916	0.867	0.886	0.906	0.911	0.913	0.915	0.874	0.902	0.880
		± 0.024	± 0.030	± 0.026	± 0.021	± 0.026	± 0.027	± 0.021	± 0.028	± 0.022	± 0.031
T ₁ \rightarrow CT	PSNR	28.01	26.92	27.26	26.94	25.61	26.75	26.55	25.14	26.38	23.72
		± 1.09	± 2.51	± 2.54	± 1.93	± 1.98	± 1.63	± 2.01	± 2.79	± 1.85	± 2.01
	SSIM	0.909	0.904	0.891	0.899	0.863	0.888	0.900	0.884	0.894	0.864
		± 0.020	± 0.029	± 0.030	± 0.027	± 0.025	± 0.028	± 0.021	± 0.026	± 0.030	± 0.032

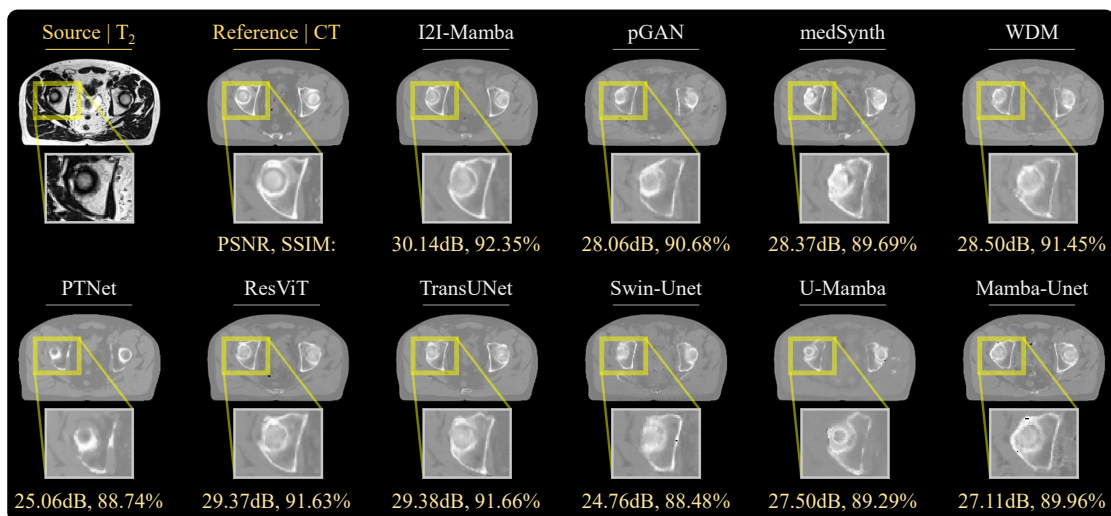


Fig. 5: Representative results for T₂ \rightarrow CT in the MRI-CT dataset. Synthetic target images from competing methods are displayed along with source images and reference target images. Zoom-in windows and error maps are also included to highlight differences among methods.

Table 4: Average inference times (Inf. in msec), memory load (Mem. in gigabytes) per cross-section and total number of parameters (Param. in millions) for competing methods.

	Inf. (ms)	Mem. (GB)	Param. (M)
I2I-Mamba	11	2.5	105.1
pGAN	9	2.3	54.4
medSynth	12	2.9	76.3
PTNet	34	10.8	280.4
ResViT	15	4.6	218.0
TransUNet	12	4.0	105.3
Swin-Unet	14	3.3	141.3
U-Mamba	10	1.6	127.8
Mamba-Unet	12	2.8	111.6
WDM	11	2.4	96.7

Table 5: Performance of I2I-Mamba variants built by: ablating ddMamba blocks (w/o ddMamba), ablating the Fourier-domain branch of ddMamba blocks (w/o ddMamba^F), ablating the image-domain branch of ddMamba blocks (w/o ddMamba^I), ablating channel-mixing layers (w/o chan mix), and ablating rCNN blocks (w/o rCNN). Results listed for representative synthesis tasks of T₁, T₂ → PD in IXI, FLAIR → T₂ in BraTS, and T₁ → CT in the MRI-CT dataset.

	T ₁ , T ₂ → PD		FLAIR → T ₂		T ₁ → CT	
	PSNR	SSIM	PSNR	SSIM	PSNR	SSIM
I2I-Mamba	33.46	0.969	25.99	0.908	28.01	0.909
	±2.52	±0.011	±2.13	±0.030	±1.09	±0.020
w/o ddMamba	32.65	0.966	24.86	0.899	27.18	0.902
	±2.56	±0.010	±2.05	±0.029	±1.98	±0.021
w/o ddMamba ^F	32.91	0.967	25.33	0.902	27.43	0.904
	±2.40	0.012	±1.56	±0.032	±1.92	±0.035
w/o ddMamba ^I	33.09	0.968	25.80	0.907	27.59	0.906
	±2.58	0.012	±2.13	±0.030	±2.06	±0.024
w/o chan mix	33.14	0.968	25.19	0.898	27.53	0.897
	±2.63	±0.012	±1.91	±0.028	±2.41	±0.028
w/o rCNN	32.69	0.966	25.07	0.894	26.60	0.885
	±2.53	±0.011	±1.83	±0.024	±2.05	±0.030

higher efficiency than transformer methods and show generally competitive efficiency to convolutional methods. Note that I2I-Mamba achieves inference time and memory usage comparable to the most efficient convolutional baselines, while its parameter count, though higher than pGAN and medSynth, remains on par with the wavelet-domain baseline (WDM). Taken together with its superior synthetic image quality, these results highlight I2I-Mamba as an efficient and effective solution for multi-modal medical image synthesis.

4.4. Ablation Studies

We performed a systematic set of ablation studies on I2I-Mamba to assess the contribution of its key design elements and configurations to synthesis performance.

Architectural components: First, we examined the importance of SSM operators in image and Fourier domains to capture spatial and spectral context, channel-mixing layers to aggregate context across the channel dimension, and rCNN blocks

Table 6: Performance of I2I-Mamba variants built by using: 1D bidirectional sweep scans (w sweep^a), 2D bidirectional sweep scans (w sweep^b), 1D bidirectional zigzag scans (w zigzag^a), 2D bidirectional zigzag scans (w zigzag^b) and ensemble sweep-zigzag scans (w sweep^a-zigzag^a).

	T ₁ , T ₂ → PD		FLAIR → T ₂		T ₁ → CT	
	PSNR	SSIM	PSNR	SSIM	PSNR	SSIM
I2I-Mamba	33.46	0.969	25.99	0.908	28.01	0.909
	±2.52	±0.011	±2.13	±0.030	±1.09	±0.020
w sweep ^a	32.72	0.964	24.97	0.891	27.31	0.890
	±2.48	0.013	±1.86	±0.031	±2.11	±0.027
w sweep ^b	32.82	0.963	25.01	0.903	27.26	0.895
	±2.49	±0.012	±1.98	±0.031	±2.58	±0.034
w zigzag ^a	32.34	0.958	24.41	0.875	26.02	0.865
	±2.77	±0.013	±1.95	±0.029	±2.17	±0.033
w zigzag ^b	32.31	0.957	24.37	0.898	26.11	0.869
	±2.65	±0.012	±1.88	±0.033	±2.25	±0.035
w sweep ^a -zigzag ^a	32.04	0.955	24.01	0.883	26.75	0.878
	±2.28	±0.011	±1.91	±0.030	±1.85	±0.029

to enhance spatial precision. I2I-Mamba was compared against several variants for this purpose: ‘w/o ddMamba’ that ablated ddMamba blocks entirely, ‘w/o ddMamba^F’ that ablated the Fourier-domain branch from the ddMamba blocks, ‘w/o ddMamba^I’ that ablated the image-domain branch from the ddMamba blocks, ‘w/o chan mix’ that ablated channel-mixing layers from ddMamba blocks, and ‘w/o rCNN’ that ablated rCNN blocks. Table 5 lists performance metrics for all variants in representative synthesis tasks. We find that I2I-Mamba consistently outperforms all variants (p<0.05), with improvements up to 1.0dB PSNR and 1.4% SSIM. These results indicate that each examined design element in I2I-Mamba contributes significantly to model performance.

Spiral-scan SSM operator: Next, we examined the importance of implementing SSM operators based on the proposed spiral-scan trajectory. For this purpose, I2I-Mamba was compared against several variants based on raster-scan trajectories (Liu et al., 2025): ‘w sweep^a’ that used 1D bidirectional sweep scans (2 separate scan trajectories), ‘w sweep^b’ that used 2D bidirectional sweep scans (4 trajectories), ‘w zigzag^a’ that used 1D bidirectional zigzag scans, ‘w zigzag^b’ that used 2D bidirectional zigzag scans, and ‘w sweep^a-zigzag^a’ that used an ensemble of sweep and zigzag scans. As listed in Table 6, we find that I2I-Mamba outperforms all variants consistently across tasks (p<0.05), with improvements up to 1.6dB PSNR and 2.3% SSIM.

Assessment of ERFs: To visually assess the influence of the spiral-scan trajectory on the SSM operator footprint, we extracted per-sample activation maps and population-average effective receptive fields (ERFs) for SSM layers (Liu et al., 2025). Fig. 6 displays activation maps and ERFs in representative cross-sections for I2I-Mamba (i.e., spiral scan), ‘w sweep^a’ (i.e., 1D bidirectional raster scans), and ‘w sweep^b’ (i.e., 2D bidirectional raster scans). We observe that I2I-Mamba significantly improves angular isotropy of the SSM operator while maintaining coverage over a broad neighborhood of pix-

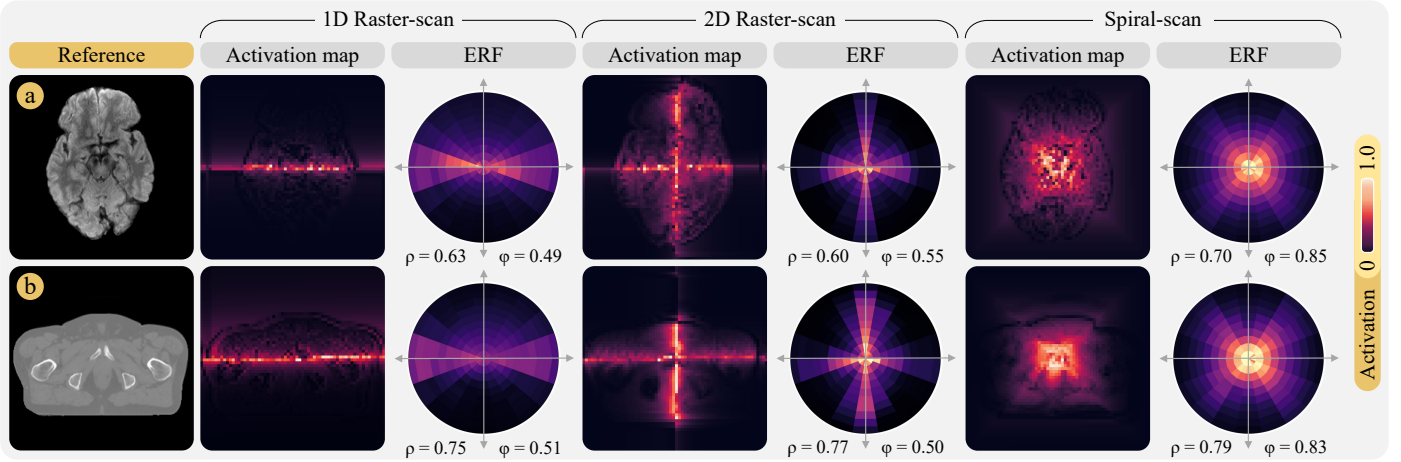


Fig. 6: Per-sample activation maps and population-average effective-receptive fields (ERF) are shown for (a) FLAIR \rightarrow T₂ in BraTS, (b) T₁ \rightarrow CT in MRI-CT. Depicting contextual interactions of a central pixel with remaining pixels across the image, activation maps and ERFs were extracted from the SSM layer at bottleneck stage $j=1$ (64×64 resolution). Results for ‘w sweep^a’ (1D bidirectional raster-scans), ‘w sweep^b’ (2D bidirectional raster-scans) and I2I-Mamba (spiral-scan), along with reference target images. For ERFs, ρ denotes the radial coverage, φ denotes the angular isotropy, both metrics normalized to a maximum of 1.

els. In contrast, ‘w sweep^a’, ‘w sweep^b’ suffer from a notable bias across the primary scan directions (i.e., horizontal and/or vertical), diminishing focus over anatomical regions distanced obliquely to the scan directions.

For quantitative assessment, ERFs were transformed into a polar representation, partitioned into 10 radial bins and 20 angular wedges. Radial coverage (ρ) was measured as the percentage of radial distances with normalized activation values above 0.1 (Fisher, 1993). Angular isotropy (φ) was measured as $1 - CV$ across orientations where CV denotes coefficient of variation (Fisher, 1993). Higher ρ reflects greater spatial spread in the ERF, hence offering enhanced sensitivity to long-range context. Meanwhile, higher φ reflects increased directional uniformity in the ERF, lowering bias towards non-axial orientations. On average across the test sets, I2I-Mamba’s ERFs show moderately higher radial coverage $\rho = 0.75$ compared to ‘w sweep^a’ with $\rho = 0.69$ and ‘w sweep^b’ with $\rho = 0.69$ ($p < 0.05$). Importantly, I2I-Mamba’s ERFs show substantially enhanced angular isotropy $\varphi = 0.84$ than both ‘w sweep^a’ with $\varphi = 0.50$ and ‘w sweep^b’ with $\varphi = 0.53$ ($p < 0.05$). Note that I2I-Mamba sustains these benefits using only a single spiral scan, compared to two scans in ‘w sweep^a’ and four scans in ‘w sweep^b’. These results indicate that the enhanced footprint of I2I-Mamba’s spiral-scan SSM operator improves its capacity to efficiently capture a more comprehensive set of contextual features in medical images, compared to conventional SSM operators.

Injection of ddMamba blocks: Lastly, we examined the importance of injecting ddMamba blocks in select stages of the bottleneck (i.e., $S = \{b1, b5, b9\}$). To do this, we compared I2I-Mamba against variants built by inserting ddMamba blocks in different configurations across the bottleneck, as well as across the encoder-decoder as listed in Table 7. While all models generally yield similar SSIM values, we find that I2I-Mamba consistently yields superior PSNR against variants ($p < 0.05$). Lower performance in variants with fewer ddMamba blocks can be attributed to a lowered ability to extract contextual features,

Table 7: Performance of I2I-Mamba variants obtained with different configurations of inserting ddMamba blocks (S). $S^* = \{b1, b5, b9\}$ denotes the configuration reported in the main experiments. e, b, d respectively denote encoder, bottleneck, and decoder stages.

	T ₁ , T ₂ \rightarrow PD		FLAIR \rightarrow T ₂		T ₁ \rightarrow CT	
	PSNR	SSIM	PSNR	SSIM	PSNR	SSIM
$S = \{b1, b2, \dots, b9\}$	33.18 ± 2.50	0.969 ± 0.011	25.72 ± 2.00	0.905 ± 0.029	27.50 ± 1.90	0.906 ± 0.024
$S = \{b1, b3, b5, b7, b9\}$	33.14 ± 2.58	0.969 ± 0.011	25.83 ± 2.07	0.907 ± 0.028	27.62 ± 2.28	0.909 ± 0.026
$S^* = \{b1, b5, b9\}$	33.46 ± 2.52	0.969 ± 0.011	25.99 ± 2.13	0.908 ± 0.030	28.01 ± 1.09	0.909 ± 0.020
$S = \{e1-e3, b1, b5, b9, d1-d3\}$	32.76 ± 2.76	0.957 ± 0.014	25.87 ± 1.92	0.908 ± 0.028	28.00 ± 2.01	0.908 ± 0.025
$S = \{b5\}$	33.09 ± 2.45	0.969 ± 0.013	25.94 ± 2.01	0.908 ± 0.027	27.84 ± 2.09	0.907 ± 0.024

whereas lower performance in variants with a greater number of ddMamba blocks is best attributed to elevated model complexity. These results suggest that I2I-Mamba attains a favorable trade-off between contextual sensitivity and model complexity via episodic injection of ddMamba blocks.

5. Discussion

5.1. Scope and Implications

In this work, we introduced I2I-Mamba, a novel state-space model (SSM)-based model for imputing missing modalities in multi-modal medical imaging. Conventional CNNs lack sensitivity to long-range dependencies across distant anatomical regions (Zhang et al., 2022), while transformer models, though better at modeling such dependencies, suffer from quadratic complexity that restricts attention to low-resolution or coarse features (Chen et al., 2024; Dalmaz et al., 2022), limiting their contextual sensitivity in high-resolution image synthesis tasks. SSMs have recently emerged as an efficient alternative, yet existing variants typically operate in the image domain

with raster-scan trajectories, which constrain their capture of global and frequency-specific context and introduce directional bias in their receptive fields across non-axial orientations. I2I-Mamba addresses these limitations via dual-domain spiral-scan SSM operators that jointly process features in the image and Fourier domains, enhancing contextual sensitivity without incurring high computational costs. Our results show that I2I-Mamba consistently outperforms CNN, transformer, and prior SSM baselines in both quantitative accuracy and visual quality.

I2I-Mamba’s performance benefits might be of value in several clinical scenarios where efficient, high-fidelity synthesis of missing modalities is needed: (i) imputing redundant but diagnostically useful target modalities to reduce total scan time; (ii) inferring invasive or high-risk modalities—such as those requiring contrast agents or ionizing radiation—using safer, non-invasive scans (Lee et al., 2019); and (iii) retrospectively recovering missing modalities to enhance harmonization across large-scale imaging datasets in population studies (Clark et al., 2019).

5.2. Limitations and Future Work

Several lines of limitations can be addressed to help further improve the proposed method’s performance. A first group of developments concerns the synthesis tasks implemented. Here we examined one-to-one and many-to-one tasks to impute missing images in multi-contrast MRI and MRI-CT protocols. For optimal performance, a separate model was built for each individual task. In certain scenarios, missing and acquired modalities in a multi-modal protocol may vary sporadically across the imaging cohort (Sharma and Hamarneh, 2020). To improve practicality, a unified I2I-Mamba can be built by adopting a masked training strategy so as to perform many-to-many synthesis tasks (Sharma and Hamarneh, 2020; Dalmaz et al., 2022). When needed, reliability of such multi-tasking models might be boosted via multi-site datasets that would provide access to larger and more diverse sets of training samples (Dalmaz et al., 2024). Here, we performed supervised learning by assuming that paired sets of source and target modality images are available in each training subject (Dar et al., 2019). In cases where it is difficult to curate paired training images, unsupervised learning strategies based on cycle-consistency could be adopted to permit training on unpaired images (Wolterink et al., 2017; Ge et al., 2019). Corroborating recent findings, here we observed high performance in translation among endogenous MRI contrasts and in translation from MRI to CT. Literature suggests that synthesizing exogenous MRI contrasts that involve external contrast agents, or synthesis of MRI images from CT are rather ill-posed problems (Lee et al., 2019; Dalmaz et al., 2022). Incorporating regularization priors regarding the distribution of the target modality might help improve synthesis fidelity in such challenging tasks (Yu et al., 2019; Lee et al., 2017).

A second group of developments concerns the employed loss functions. For fair comparison, here we implemented all competing methods based on a combined pixel-wise/adversarial loss (Dalmaz et al., 2022). While we observed that this learning approach elicits high-quality synthetic images, further improvements might be viable with advanced loss terms including gradient-based, difficulty-aware, cross-entropy losses (Nie

et al., 2018; Zhan et al., 2021; Nie and Shen, 2020). A potential limitation of adversarial learning is instabilities in model training that can hamper the fidelity of synthetic images (Özbey et al., 2023). While here we did not observe signs of instability in model training, diffusion learning could be adopted to improve reliability when necessary (Arslan et al., 2024; Ju and Zhou, 2024). Additional improvements to be sought for a diffusion-based implementation include bridge formulations to boost task-relevant information (Korkmaz et al., 2023). Lastly, synthesis performance might be further improved by adopting model pre-training procedures. Future studies are warranted for an in-depth evaluation of the ideal training procedures for I2I-Mamba.

6. Conclusion

In this study, we proposed a novel learning-based method for imputing missing modalities in multi-modal medical imaging protocols. To improve fidelity in synthetic images, I2I-Mamba leverages a novel SSM-based architecture with dual-domain Mamba blocks operating in image and Fourier domains to capture spatial and spectral contextual features. These ddMamba blocks are further equipped with spiral-scan trajectories to improve angular isotropy in the receptive field of SSM operators. With its superior performance and competitive computational efficiency with respect to state-of-the-art baselines, I2I-Mamba holds great potential for multi-modal medical image synthesis.

Data Availability

The public repositories containing the data analyzed in this study have been listed in the manuscript. The code is publicly available at: <https://github.com/icon-lab/I2I-Mamba>.

Acknowledgment

This work was supported in part by The Scientific and Technological Research Council of Türkiye (TÜBİTAK) 1515 Frontier R&D Laboratories Support Program for Türk Telekom 6G R&D Lab under project number 5249902.

References

- Adam, A., Dixon, A., Gillard, J., Schaefer-Prokop, C., Grainger, R., Allison, D., 2014. Grainger & Allison’s Diagnostic Radiology. Elsevier.
- Alexander, D.C., Zikic, D., Zhang, J., Zhang, H., Criminisi, A., 2014. Image quality transfer via random forest regression: Applications in diffusion MRI, in: MICCAI, pp. 225–232.
- Armanious, K., Jiang, C., Fischer, M., Küstner, T., Hepp, T., Nikolaou, K., Gatidis, S., Yang, B., 2019. MedGAN: Medical image translation using GANs. *Comput Med Imaging Graph* 79, 101684.
- Arslan, F., Kabas, B., Dalmaz, O., Ozbey, M., Çukur, T., 2024. Self-consistent recursive diffusion bridge for medical image translation. *arXiv:2405.06789*.
- Atli, O.F., Kabas, B., Arslan, F., Demirtas, A.C., Yurt, M., Dalmaz, O., Çukur, T., 2024. I2I-Mamba: Multi-modal medical image synthesis via selective state space modeling. *arXiv:2405.14022*.

- Baid, U., Ghodasara, S., Mohan, S., Bilello, M., Calabrese, E., Colak, E., Farahani, K., Kalpathy-Cramer, J., Kitamura, F.C., Pati, S., Prevedello, L.M., Rudie, J.D., Sako, C., Shinohara, R.T., Bergquist, T., Chai, R., Eddy, J., Elliott, J., Reade, W., Schaffter, T., Yu, T., Zheng, J., Moawad, A.W., Coelho, L.O., McDonnell, O., Miller, E., Moron, F.E., Oswood, M.C., Shih, R.Y., Siakallis, L., Bronstein, Y., Mason, J.R., Miller, A.F., Choudhary, G., Agarwal, A., Besada, C.H., Derakhshan, J.J., Diogo, M.C., Do-Dai, D.D., Farage, L., Go, J.L., Hadi, M., Hill, V.B., Iv, M., Joyner, D., Lincoln, C., Lotan, E., Miyakoshi, A., Sanchez-Montano, M., Nath, J., Nguyen, X.V., Nicolas-Jilwan, M., Jimenez, J.O., Ozturk, K., Petrovic, B.D., Shah, C., Shah, L.M., Sharma, M., Simsek, O., Singh, A.K., Soman, S., Statevych, V., Weinberg, B.D., Young, R.J., Ikuta, I., Agarwal, A.K., Cambron, S.C., Silbergleit, R., Dusoi, A., Postma, A.A., Letourneau-Guillon, L., Perez-Carrillo, G.J.G., Saha, A., Soni, N., Zaharchuk, G., Zohrabian, V.M., Chen, Y., Cekic, M.M., Rahman, A., Small, J.E., Sethi, V., Davatzikos, C., Mongan, J., Hess, C., Cha, S., Villanueva-Meyer, J., Freymann, J.B., Kirby, J.S., Wiestler, B., Crivellaro, P., Colen, R.R., Kotrotsou, A., Marcus, D., Milchenko, M., Nazari, A., Fathallah-Shaykh, H., Wiest, R., Jakab, A., Weber, M.A., Mahajan, A., Menze, B., Flanders, A.E., Bakas, S., 2021. The rsna-asnr-miccai brats 2021 benchmark on brain tumor segmentation and radiogenomic classification. *arXiv:2107.02314*.
- Bedel, H.A., Sivgin, I., Dalmaz, O., Dar, S.U., Çukur, T., 2023. Bolt: Fused window transformers for fmri time series analysis. *Med Image Anal* 88, 102841.
- Beers, A., Brown, J., Chang, K., Campbell, J., Ostmo, S., Chiang, M., Kalpathy-Cramer, J., 2018. High-resolution medical image synthesis using progressively grown generative adversarial networks. *arXiv:1805.03144*.
- Bilgic, B., Goyal, V.K., Adalsteinsson, E., 2011. Multi-contrast reconstruction with Bayesian compressed sensing. *Magn Reson Med* 66, 1601–1615.
- Bowles, C., Qin, C., Ledig, C., Guerrero, R., Gunn, R., Hammers, A., Sakka, E., Dickie, D., Hernández, M., Royle, N., Wardlaw, J., Rhodus-Meester, H., Tijms, B., Lemstra, A., Flier, W., Barkhof, F., Scheltens, P., Rueckert, D., 2016. Pseudo-healthy image synthesis for white matter lesion segmentation. *in: SSMI*, pp. 87–96.
- Cao, H., Wang, Y., Chen, J., Jiang, D., Zhang, X., Tian, Q., Wang, M., 2022. Swin-unet: Unet-like pure transformer for medical image segmentation. *in: Proc ECCV*.
- Chartsias, A., Joyce, T., Giuffrida, M.V., Tsaftaris, S.A., 2018. Multimodal MR synthesis via modality-invariant latent representation. *IEEE Trans Med Imaging* 37, 803–814.
- Chen, J., Mei, J., Li, X., Lu, Y., Yu, Q., Wei, Q., Luo, X., Xie, Y., Adeli, E., Wang, Y., Lungren, M.P., Zhang, S., Xing, L., Lu, L., Yuille, A., Zhou, Y., 2024. Transunet: Rethinking the u-net architecture design for medical image segmentation through the lens of transformers. *Med Image Anal* 97, 103280.
- Chen, S., Zhang, R., Liang, H., Qian, Y., Zhou, X., 2025. Coupling of state space modules and attention mechanisms: An input-aware multi-contrast mri synthesis method. *Med Phys* 52, 2269–2278.
- Clark, L.T., Watkins, L., Pina, I.L., Elmer, M., Akinboboye, O., Gorham, M., Jamerson, B., McCullough, C., Pierre, C., Polis, A.B., Puckrein, G., Regnante, J.M., 2019. Increasing Diversity in Clinical Trials: Overcoming Critical Barriers. *Cur. Prob. Cardiol.* 44, 148–172.
- Dalmaz, O., Mirza, M.U., Elmas, G., Ozbey, M., Dar, S.U., Ceyani, E., Oguz, K.K., Avestimehr, S., Çukur, T., 2024. One model to unite them all: Personalized federated learning of multi-contrast MRI synthesis. *Med Image Anal* 94, 103121.
- Dalmaz, O., Yurt, M., Çukur, T., 2022. ResViT: Residual vision transformers for multi-modal medical image synthesis. *IEEE Trans Med Imaging* 44, 2598–2614.
- Dar, S.U., Yurt, M., Karacan, L., Erdem, A., Erdem, E., Çukur, T., 2019. Image synthesis in multi-contrast MRI with conditional generative adversarial networks. *IEEE Trans Med Imaging* 38, 2375–2388.
- Fisher, N.I., 1993. *Statistical Analysis of Circular Data*. Cambridge University Press.
- Friedrich, P., Wolleb, J., Bieder, F., Durrer, A., Cattin, P.C., 2025. Wdm: 3d wavelet diffusion models for high-resolution medical image synthesis. *in: DGM4MICCAI*, pp. 11–21.
- Ge, Y., Wei, D., Xue, Z., Wang, Q., Zhou, X., Zhan, Y., Liao, S., 2019. Unpaired MR to CT synthesis with explicit structural constrained adversarial learning. *in: ISBI*, pp. 1096–1099.
- He, K., Zhang, X., Ren, S., Sun, J., 2016. Deep residual learning for image recognition. *in: CVPR*, pp. 770–778.
- Huang, J., Yang, L., Wang, F., Wu, Y., Nan, Y., Wu, W., Wang, C., Shi, K., Aviles-Rivero, A.I., Schönlieb, C.B., Zhang, D., Yang, G., 2025. Enhancing global sensitivity and uncertainty quantification in medical image reconstruction with monte carlo arbitrary-masked mamba. *Med Image Anal* 99, 103334.
- Huang, Y., Shao, L., Frangi, A.F., 2017. Simultaneous super-resolution and cross-modality synthesis of 3D medical images using weakly-supervised joint convolutional sparse coding. *in: CVPR*, pp. 5787–5796.
- Huo, Y., Xu, Z., Bao, S., Assad, A., Abramson, R.G., Landman, B.A., 2018. Adversarial synthesis learning enables segmentation without target modality ground truth. *in: ISBI*, pp. 1217–1220.
- Huynh, T., Gao, Y., Kang, J., Wang, L., Zhang, P., Lian, J., Shen, D., 2016. Estimating CT image from MRI data using structured random forest and auto-context model. *IEEE Trans Med Imaging* 35, 174–183.
- Iglesias, J.E., Konukoglu, E., Zikic, D., Glocker, B., Van Leemput, K., Fischl, B., 2013. Is synthesizing MRI contrast useful for inter-modality analysis?. *in: MICCAI*, pp. 631–638.
- Joyce, T., Chartsias, A., Tsaftaris, S.A., 2017. Robust multi-modal MR image synthesis. *in: MICCAI*, pp. 347–355.
- Ju, Z., Zhou, W., 2024. Vm-ddpm: Vision mamba diffusion for medical image synthesis. *arXiv:2405.05667*.
- Korkmaz, Y., Cukur, T., Patel, V.M., 2023. Self-supervised mri reconstruction with unrolled diffusion models. *in: MICCAI*, pp. 491–501.
- Korkmaz, Y., Patel, V.M., 2025. Mambarecon: Mri reconstruction with structured state space models. *in: IEEE/CVF WACV*, pp. 4142–4152.
- Lan, H., Toga, A., Sepehrband, F., 2020. SC-GAN: 3D self-attention conditional GAN with spectral normalization for multi-modal neuroimaging synthesis. *bioRxiv:2020.06.09.143297*.
- Lee, D., Kim, J., Moon, W.J., Ye, J.C., 2019. CollaGAN: Collaborative GAN for missing image data imputation. *in: CVPR*, pp. 2487–2496.
- Lee, J., Carass, A., Jog, A., Zhao, C., Prince, J., 2017. Multi-atlas-based CT synthesis from conventional MRI with patch-based refinement for MRI-based radiotherapy planning. *in: SPIE Med. Imag.*, p. 1013311.
- Li, H., Paetzold, J.C., Sekuboyina, A., Kofler, F., Zhang, J., Kirschke, J.S., Wiestler, B., Menze, B., 2019. DiamondGAN: Unified multi-modal generative adversarial networks for MRI sequences synthesis. *in: MICCAI*, pp. 795–803.
- Li, Y., Zhou, T., He, K., Zhou, Y., Shen, D., 2023. Multi-scale transformer network with edge-aware pre-training for cross-modality mr image synthesis. *IEEE Trans Med Imaging* 42, 3395–3407.
- Liu, J., Pasumarthi, S., Duffy, B., Gong, E., Datta, K., Zaharchuk, G., 2023. One Model to Synthesize Them All: Multi-Contrast Multi-Scale Transformer for Missing Data Imputation. *IEEE Trans Med Imaging* 42, 2577–2591.
- Liu, Y., Tian, Y., Zhao, Y., Yu, H., Xie, L., Wang, Y., Ye, Q., Liu, Y., 2025. Vmamba: Visual state space model. *in: NeurIPS*.
- Ma, C., Wang, Z., 2024. Semi-mamba-unet: Pixel-level contrastive and cross-supervised visual mamba-based unet for semi-supervised medical image segmentation. *Knowled Syst* 300, 112203.
- Ma, J., Li, F., Wang, B., 2024. U-mamba: Enhancing long-range dependency for biomedical image segmentation. *arXiv:2401.04722*.
- Nie, D., Shen, D., 2020. Adversarial Confidence Learning for Medical Image Segmentation and Synthesis. *Int J Comput. Vision* 128, 2494–2513.
- Nie, D., Trullo, R., Lian, J., Wang, L., Petitjean, C., Ruan, S., Wang, Q., Shen, D., 2018. Medical image synthesis with deep convolutional adversarial networks. *IEEE Trans Biomed Eng* 65, 2720–2730.
- Nyholm, T., Svensson, S., Andersson, S., Jonsson, J., Sohlén, M., Gustafsson, C., Kjellén, E., Söderström, K., Albertsson, P., Blomqvist, L., Zackrisson, B., Olsson, L.E., Gunnlaugsson, A., 2018. MR and CT data with multi-observer delineations of organs in the pelvic area—part of the gold atlas project. *Med Phys* 45, 1295–1300.
- Oktaç, O., Schlemper, J., Folgoc, L.L., Lee, M.J., Heinrich, M., Misawa, K., Mori, K., McDonagh, S.G., Hammerla, N., Kainz, B., Glocker, B., Rueckert, D., 2018. Attention U-Net: Learning where to look for the pancreas. *arXiv:1804.03999*.
- Özbeý, M., Dar, S.U., Bedel, H.A., Dalmaz, O., Özturk, Ş., Güngör, A., Çukur, T., 2023. Unsupervised medical image translation with adversarial diffusion models. *IEEE Trans Med Imaging* 42, 3524–3539.
- Pichler, B.J., Judenhofer, M.S., Pfannenberger, C., 2008. *Multimodal Imaging Approaches: PET/CT and PET/MRI*. Springer. pp. 109–132.
- Sharma, A., Hamarneh, G., 2020. Missing MRI pulse sequence synthesis using multi-modal generative adversarial network. *IEEE Trans Med Imaging* 39,

1170–1183.

- Shin, H.C., Ihsani, A., Mandava, S., Sreenivas, S.T., Forster, C., Cha, J., Initiative, A.D.N., 2020. GANBERT: Generative adversarial networks with bidirectional encoder representations from transformers for MRI to PET synthesis. arXiv:2008.04393 .
- Thukral, B., 2015. Problems and preferences in pediatric imaging. *Ind J Rad Imaging* 25, 359–364.
- Tolstikhin, I., Houlsby, N., Kolesnikov, A., Beyer, L., Zhai, X., Unterthiner, T., Yung, J., Steiner, A., Keysers, D., Uszkoreit, J., Lucic, M., Dosovitskiy, A., 2021. Mlp-mixer: An all-mlp architecture for vision, in: *NeurIPS*.
- Vemulapalli, R., Van Nguyen, H., Zhou, S.K., 2015. Unsupervised cross-modal synthesis of subject-specific scans, in: *ICCV*, pp. 630–638.
- Wang, G., Gong, E., Banerjee, S., Martin, D., Tong, E., Choi, J., Chen, H., Wintermark, M., Pauly, J.M., Zaharchuk, G., 2020. Synthesize high-quality multi-contrast magnetic resonance imaging from multi-echo acquisition using multi-task deep generative model. *IEEE Trans Med Imaging* 39, 3089–3099.
- Wei, W., Poirion, E., Bodini, B., Durrleman, S., Colliot, O., Stankoff, B., Ayache, N., 2019. Fluid-attenuated inversion recovery MRI synthesis from multisequence MRI using three-dimensional fully convolutional networks for multiple sclerosis. *J Med Imaging* 6, 014005.
- Wolterink, J., Dinkla, A.M., Savenije, M., Seevinck, P., Berg, C., Isgum, I., 2017. Deep MR to CT synthesis using unpaired data, in: *SSMI*, pp. 14–23.
- Wu, Y., Yang, W., Lu, L., Lu, Z., Zhong, L., Huang, M., Feng, Y., Feng, Q., Chen, W., 2016. Prediction of CT substitutes for MR images based on local diffeomorphic mapping for brain PET attenuation correction. *J Nuc Med* 57, 1635–1641.
- Yang, H., Sun, J., Carass, A., Zhao, C., Lee, J., Xu, Z., Prince, J., 2020. Unpaired brain MR-to-CT synthesis using a structure-constrained cycleGAN. *IEEE Trans Med Imaging* 39, 4249–4261.
- Yu, B., Zhou, L., Wang, L., Frripp, J., Bourgeat, P., 2018. 3D cGAN based cross-modality MR image synthesis for brain tumor segmentation, in: *ISBI*, pp. 626–630.
- Yu, B., Zhou, L., Wang, L., Shi, Y., Frripp, J., Bourgeat, P., 2019. Ea-gans: edge-aware generative adversarial networks for cross-modality mr image synthesis. *IEEE Trans Med Imaging* 38, 1750–1762.
- Yuan, Z., Jiang, M., Wang, Y., Wei, B., Li, Y., Wang, P., Menpes-Smith, W., Niu, Z., Yang, G., 2020. SARA-GAN: Self-attention and relative average discriminator based generative adversarial networks for fast compressed sensing MRI reconstruction. *Front Neuroinform* 14, 58.
- Yurt, M., Dar, S.U., Erdem, A., Erdem, E., Oguz, K.K., Çukur, T., 2021. must-GAN: multi-stream generative adversarial networks for MR image synthesis. *Med Image Anal* 70, 101944.
- Zhan, B., Li, D., Wang, Y., Ma, Z., Wu, X., Zhou, J., Zhou, L., 2021. LR-cGAN: Latent representation based conditional generative adversarial network for multi-modality MRI synthesis. *Biomed. Signal Process. Control* 66, 102457.
- Zhang, X., He, X., Guo, J., Etehad, N., Aw, N., Semanek, D., Posner, J., Laine, A., Wang, Y., 2022. PTNet3D: A 3D High-Resolution Longitudinal Infant Brain MRI Synthesizer Based on Transformers. *IEEE Trans Med Imaging* 41, 2925–2940.
- Zhao, C., Carass, A., Lee, J., He, Y., Prince, J.L., 2017. Whole brain segmentation and labeling from CT using synthetic MR images, in: *MLMI*, pp. 291–298.
- Zhao, J., Li, D., Kassam, Z., Howey, J., Chong, J., Chen, B., Li, S., 2020. Tripartite-GAN: Synthesizing liver contrast-enhanced MRI to improve tumor detection. *Med Image Anal* 63, 101667.
- Zhou, T., Fu, H., Chen, G., Shen, J., Shao, L., 2020. Hi-Net: Hybrid-fusion network for multi-modal MR image synthesis. *IEEE Trans Med Imaging* 39, 2772–2781.
- Zhu, L., Liao, B., Zhang, Q., Wang, X., Liu, W., Wang, X., 2024. Vision mamba: Efficient visual representation learning with bidirectional state space model, in: *ICML*.